KeAi

CHINESE ROOTS
GLOBAL IMPACT

#### Contents lists available at ScienceDirect

## Petroleum Science

journal homepage: www.keaipublishing.com/en/journals/petroleum-science



## Original Paper

## Evolution and generation mechanism of retained oil in lacustrine shales: A combined ReaxFF-MD and pyrolysis simulation perspective



Biao Sun <sup>a, b</sup>, Xiao-Ping Liu <sup>a, b, \*</sup>, Jie Liu <sup>c</sup>, Tian Liu <sup>a, b</sup>, Zu-Xian Hua <sup>a, b</sup>, Wen-Di Peng <sup>a, b</sup>

- <sup>a</sup> National Key Laboratory of Petroleum Resources and Engineering, China University of Petroleum (Beijing), Beijing, 102249, China
- b College of Geosciences, China University of Petroleum (Beijing), Beijing, 102249, China
- <sup>c</sup> International Petroleum Exploration and Production Corporation, SINOPEC, Beijing, 100029, China

#### ARTICLE INFO

# Article history: Received 8 February 2024 Received in revised form 2 June 2024 Accepted 23 July 2024 Available online 24 July 2024

Edited by Jie Hao and Meng-Jiao Zhou

Keywords:
Lacustrine shale
Retained oiliness evolution
Pyrolysis simulation experiments
ReaxFF molecular dynamics
Hydrocarbon generation evolution

#### ABSTRACT

To accurately investigate the evolution characteristics and generation mechanism of retained oil, the study analyzed organic-rich lacustrine shale samples from the Paleogene Kongdian Formation in Cangdong Sag, Bohai Bay Basin. This analysis involves Rock-Eval pyrolysis, pyrolysis simulation experiments, Gas Chromatograph Mass Spectrometer (GC-MS), and reactive molecular dynamics simulations (ReaxFF). The results revealed the retained oil primarily consisted of n-alkanes with carbon numbers ranging from C<sub>14</sub> to C<sub>36</sub>. The generation of retained oil occurred through three stages. A slow growth stage of production rate was observed before reaching the peak of oil production in Stage I. Stage II involved a rapid increase in oil retention, with  $C_{12}$ – $C_{17}$  and  $C_{24}$ – $C_{32}$  serving as the primary components, increasing continuously during the pyrolysis process. The generation process involved the cleavage of weak bonds, including bridging bonds (hydroxyl, oxy, peroxy, imino, amino, and nitro), ether bonds, and acid amides in the first stage ( $R_0 = 0.50\% - 0.75\%$ ). The carbon chains in aromatic ring structures with heteroatomic functional groups breaks in the second stage ( $R_0 = 0.75\%-1.20\%$ ). In the third stage  $(R_0 = 1.20\% - 2.50\%)$ , the ring structures underwent ring-opening reactions to synthesize iso-short-chain olefins and radicals, while further breakdown of aliphatic chains occurred. By coupling pyrolysis simulation experiments and molecular simulation technology, the evolution characteristics and bond breaking mechanism of retained oil in three stages were revealed, providing a reference for the formation and evolution mechanism of retained oil.

© 2025 The Authors. Publishing services by Elsevier B.V. on behalf of KeAi Communications Co. Ltd. This is an open access article under the CC BY-NC-ND license (http://creativecommons.org/licenses/by-nc-nd/4.0/).

## 1. Introduction

Terrestrial shale oil plays a crucial role as an unconventional oil resource (Jin et al., 2021; Dunkel et al., 2022; Goodarzi, 2020; Hail et al., 2023). In China, significant advancements have been made in the exploration of terrestrial shale oil, particularly in the Junggar Basin (Olariu et al., 2022), Ordos Basin (Fu et al., 2020;Xi et al., 2020; Hou et al., 2022), Songliao Basin (Horsfield et al., 2022; Jin et al., 2022), and Bohai Bay Basin (Li et al., 2019; Zhao et al., 2022). However, the development of shale oil in these regions has been impacted by various challenges, including non-homogeneity, limited mobility, and poor fracturability (Jin et al., 2018; Amine

et al., 2022; Hail et al., 2023). Consequently, it is important to note that the quantitative evaluation and understanding of the formation mechanism of retained oil are crucial factors that hinder the efficient development of shale oil.

The composition of retained oil is a critical internal factor influencing the oil content and mobility of shale oil. The occurrence states of retained oil can be classified into free oil, irreducible oil and adsorbed oil. The free oil is mainly composed of light components of hydrocarbon, while the heavy components of irreducible oil and absorbed oil increase (Zhang et al., 2023; Li et al., 2024) which is primarily controlled by the thermal evolution of hydrocarbon generation within the reservoir (Arvelos et al., 2019; Li et al., 2022). With advancements in experimental techniques, numerous scholars have utilized a wide range of physical and simulation tools to explore the components and evolutionary characteristics of hysteretic oil (Liu et al., 2020; Li et al., 2022). In general, three main types of methods are commonly adopted for evaluating hysteretic

<sup>\*</sup> Corresponding author. National Key Laboratory of Petroleum Resources and Engineering, China University of Petroleum (Beijing), Beijing, 102249, China. E-mail address: liuxiaoping@cup.edu.cn (X.-P. Liu).

oil content in shale: direct observation, experimental analysis, and molecular dynamics simulation (Salmon et al., 2009; Saif et al., 2017; Al et al., 2022). Specifically, thermal simulation experiments have emerged as a primary technical means of evaluating retained oil content. In terms of confinement, there are three main categories: open system, semi-open system, and confined system. Among these, the semi-confined condition closely resembles the formation condition and is particularly useful for studying retained oil (Barnie et al., 2022; Omari et al., 2022; Wang et al., 2022). ReaxFF MD is a significant method used for representing reactions in shale oil systems. It is a valuable tool for calculating complex reactions in large-scale systems and has been used in the pyrolysis of coal, oil shale, and other processes, as well as in studying reaction mechanisms (Al et al., 2022). However, it is important to note that molecular simulations cannot replace experimental data and should be calibrated and analyzed against experimental results. The evolution and formation mechanism of retained oil in terrestrial shale has posed challenges for the efficient development of shale oil. Additionally, the evolution process and formation mechanism of retained oil under specific stratigraphic conditions have been rarely explored. Therefore, this study aims to investigate the evolution and formation mechanism of retained oil during shale caseous root pyrolysis using thermal simulation experiments and the ReaxFF MD simulation method.

The study selected a sample of type I kerogen from the Bohai Bay Basin and examined the evolution and formation mechanism of retained oil through various techniques such as Pyrolysis simulation experiments, pyrolysis-gas chromatography/mass spectrometry (Py-GC/MS), X-ray Diffraction (XRD), total organic carbon content (TOC), vitrinite reflectance ( $R_0$ ), Rock-Eval pyrolysis, and ReaxFF. By analyzing the evolution characteristics of retained oil and in-depth understanding of its generation mechanism, this study combines ReaxFF-MD simulation with pyrolysis simulation experiments to propose the thermal evolution stages and formation mechanism of retained oil enrichment in lacustrine shale oil, and provides information on lacustrine shale retained oil and favorable intervals and target areas for shale oil exploration. The successful exploration of the Ek2 in the Cangdong Sag shows that lacustrine shale has huge potential for retained oil resources. However, due to the strong heterogeneity of lacustrine shale lithofacies and the existence of formation media, which may affect the formation and enrichment of retained oil, these effects will continue to be studied. These findings help to better understand the evolution and formation mechanism of retained oil and provide insights for the efficient development of lacustrine shale oil.

#### 2. Geological setting

The Huanghua Sub-basin, located in the center of the Bohai Bay Basin, is divided into two distinct secondary subsidence units: the Cangdong Sag in the south and the Qikou Sag in the north, with the Kongdian-Yangsanmu Uplift acting as the boundary. The Cangdong Sag, in particular, has been identified as the second largest oil-rich depression in the area. This narrow Cenozoic fault basin formed due to regional tension from the southwest to the northeast and spans an exploration area of approximately 1.8  $\times$  10 $^3$  km $^2$  (Fig. 1) (Zhao et al., 2019, 2022). The Paleogene system within the Cangdong Sag consists of three main sets of strata: the Kongdian Formation, the Shahejie Formation, and the Dongying Formation. Specifically, the Kongdian Formation can be further divided into the Ek<sub>1</sub>, Ek<sub>2</sub>, and Ek<sub>3</sub> submembers (Fig. 2). The Ek<sub>2</sub> subunit is characterized by dominant sandstone sedimentation at the lake basin

margin, while the middle of the lake basin features semi-deep lacustrine and deep organic-rich shale sedimentation covering an area of approximately  $2.6\times10^2~\text{km}^2$  (Zhao et al., 2018). In terms of organic matter content, the shale system in the Ek<sub>2</sub> subunit exhibits a range of 0.3%-11.9% (average 3.6%). The average hydrocarbon potential, represented by the sum of S<sub>1</sub> and S<sub>2</sub>, is 18.9 mg/g, indicating a high hydrocarbon-rich source rock with maturity levels ranging from 0.66% to 0.96%. The dense shale system in this section can serve as an effective reservoir and is considered a crucial target for shale oil development in the Cangdong Sag (Pu et al., 2016; Zhou et al., 2020).

#### 3. Samples and methods

#### 3.1. Samples

Shale samples from Well G9 (Fig. 2) were collected to conduct a systematic analysis of retained oil evolution characteristics. Table 1 provides specific information about the samples. The sample analysis took place at China University of Petroleum (Beijing), where the samples underwent XRD, TOC, and  $R_{\rm 0}$  analyses. The pyrolysis simulation experiments were carried out at Wuxi Research Institute of Petroleum Geology. It is worth noting that the pyrolysis simulation experiments focused on shale samples characterized by high TOC and low maturity levels.

#### 3.2. Experiments

To gain a deeper understanding of the hydrocarbon generation, expulsion and retention pattern of organic-rich lacustrine shale under stratigraphic conditions, the hydrocarbon generation and expulsion simulator developed by Wuxi Research Institute of Petroleum Geology was utilized. The specific equipment employed in this study is the DK-II formation pore thermal compression hydrocarbon generation and expulsion simulation experiment instrument. This multifunctional simulator consists of several components, including a high-temperature and high-pressure hydrocarbon generation reaction system, a two-way hydraulic control system, a hydrocarbon expulsion system, an automatic control and data acquisition system, a product separation and collection system, as well as peripheral auxiliary equipment and an instrument shell (Liu et al., 2015).

The simulator offers the advantage of preserving the original mineral composition structure and organic matter characteristics of the hydrocarbon source rock, while considering the pyrolysis of organic matter and hydrocarbon generation reactions under higher rock pressure, stratigraphic fluid pressure, and surrounding pressure, mimicking geological conditions.

For this study, temperatures were set at 573.15, 598.15, 623.15, 648.15, 673.15, 773.15 K to analyze the different stages of retained oil formation. The samples were in the low-mature stage before reaching 598.15 K, transitioning to the mature stage between temperatures of 598.15 K and 648.15 K. The high-mature stage, also known as the wet gas phase, occurred between 648.15 K and 673.15 K, while the over-mature stage was associated with temperatures between 673.15 K and 773.15 K (Dong et al., 2013; Liu et al., 2022; Ma et al., 2022). The formation and lithostatic pressures were set to replicate the actual pressure conditions of the Ek2 shale. Additionally, experimental hydrostatic pressures were established using fictitious burial depths (Liu et al., 2022).

In general, the process of simulating hydrocarbon generation and expulsion from limited space of hydrocarbon source rock

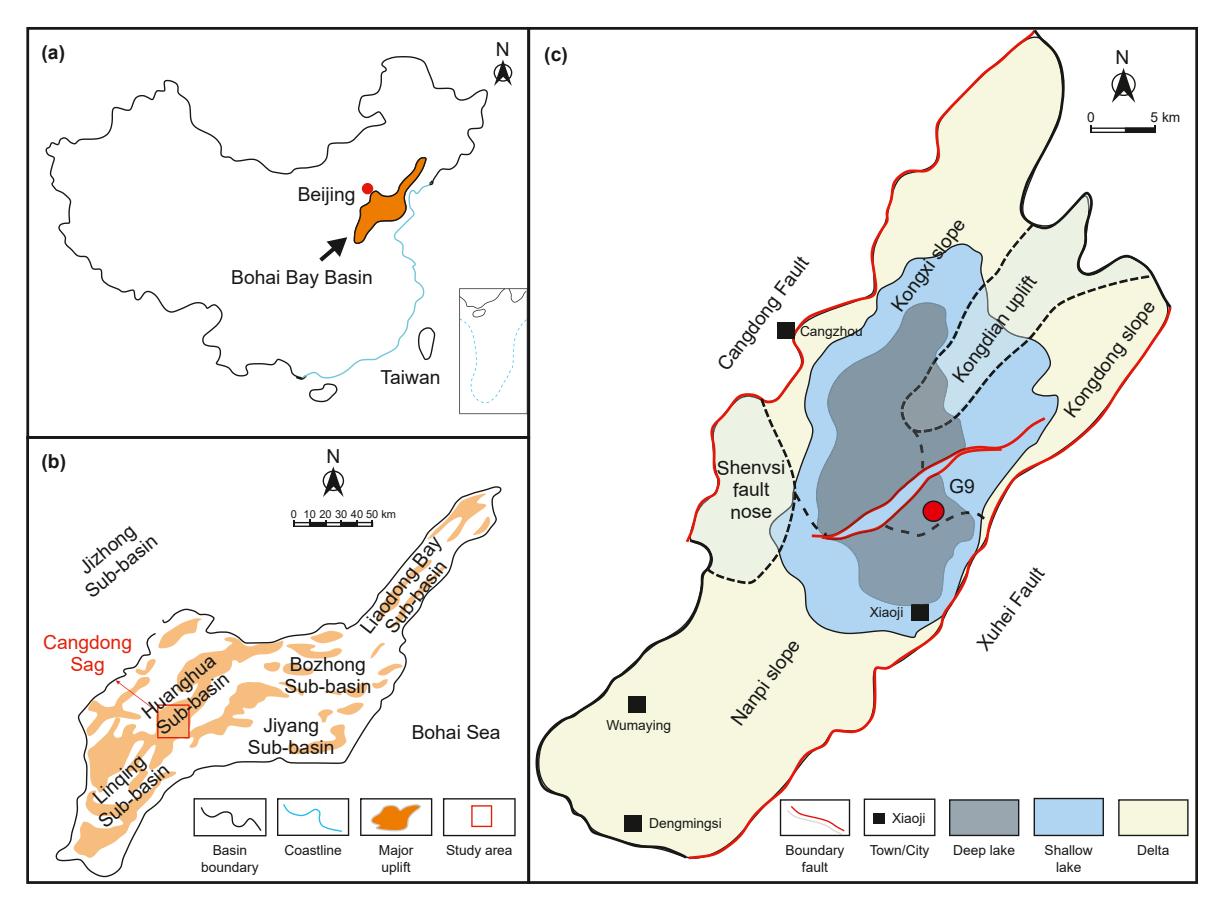


Fig. 1. Location and tectonic units of the study area. (a) Location of Bohai Bay Basin; (b) division of basic structural units of Bohai Bay Basin; (c) geological sketch map and the sedimentary facies of the Cangdong Sag showing the location of the sampling well.

involves several steps including sample preparation, loading, temperature and pressure simulation, sampling, product geochemical analysis, and other procedures.

Firstly, for sample preparation and loading, core columns (35 mm length) were obtained from the core according to the experimental equipment size. Next, temperature and pressure simulation were carried out. The process involved testing for leaks by sealing the sample in a reaction vessel, injecting inert gas, and then vacuum pumping. Water injection was also performed using a high-pressure pump to ensure the reaction space was filled adequately. Following that, compaction and warming procedures were conducted. The sample was compacted for heating and the simulation experiment was performed at a constant temperature for 48 h.

Product collection and analysis were then carried out. Gas and discharge oil were collected after the reaction process. Gas analysis was performed using a gas chromatograph to determine the mass of various gas substances. Additionally, remaining solids and lingering oil samples were extracted using asphalt "A" and chloroform. Total oil was calculated by combining the residual and discharge oil, while total hydrocarbon was determined by adding hydrocarbon gas to the total oil. The discharged oil was separated from the residual oil using column chromatography with four racial components. The quantitatively separated results were then analyzed using GC-MS.

In routine pyrolysis experiments, approximately 70 mg of the powdered sample was used with a Rock-Eval 6 device to determine various pyrolysis parameters such as free hydrocarbon ( $S_1$ ), thermal cracking hydrocarbon ( $S_2$ ), peak temperature ( $T_{max}$ ), and hydrogen

index (HI). Lastly, in the GC-MS experiments, asphaltenes were precipitated from the extracts and expelled oil using n-hexane. The aliphatic, aromatic, and resin fractions were then separated using a chromatographic column and different irrigating agents. The aliphatic components were analyzed using an Agilent 7890 gas chromatograph.

#### 3.3. ReaxFF-MD methods

#### 3.3.1. Molecular models

The molecular dynamics (MD) of kerogen pyrolysis was investigated using ReaxFF in the LAMMPS software. The kerogen model employed in this study was based on the description by Ungerer et al. The chemical formula of the model is  $C_{251}H_{385}O_{13}N_7S_3$  (Fig. 3) (Ungerer et al., 2015). At present, the structure of kerogen is complex and diverse, but the kerogen in this study and the kerogen model of the Green River Formation are similar in depositional environment, organic matter source, functional group composition, and thermal evolution stage. Therefore, the kerogen model of the Green River Formation was chosen as a molecular model.

To simulate pyrolysis using ReaxFF, a kerogen model was constructed by optimizing the geometry of different configurations generated through simulated annealing with the Forcite calculation module in MS software. The structure with the minimum energy was then used for ReaxFF reactive molecular dynamics simulations (Castro-Marcano et al., 2014; Wang et al., 2020). ReaxFF is an empirical bond-order-based reactive force field that effectively describes bond cleavage and formation during chemical reactions. It allows for clear characterization of chemical processes within

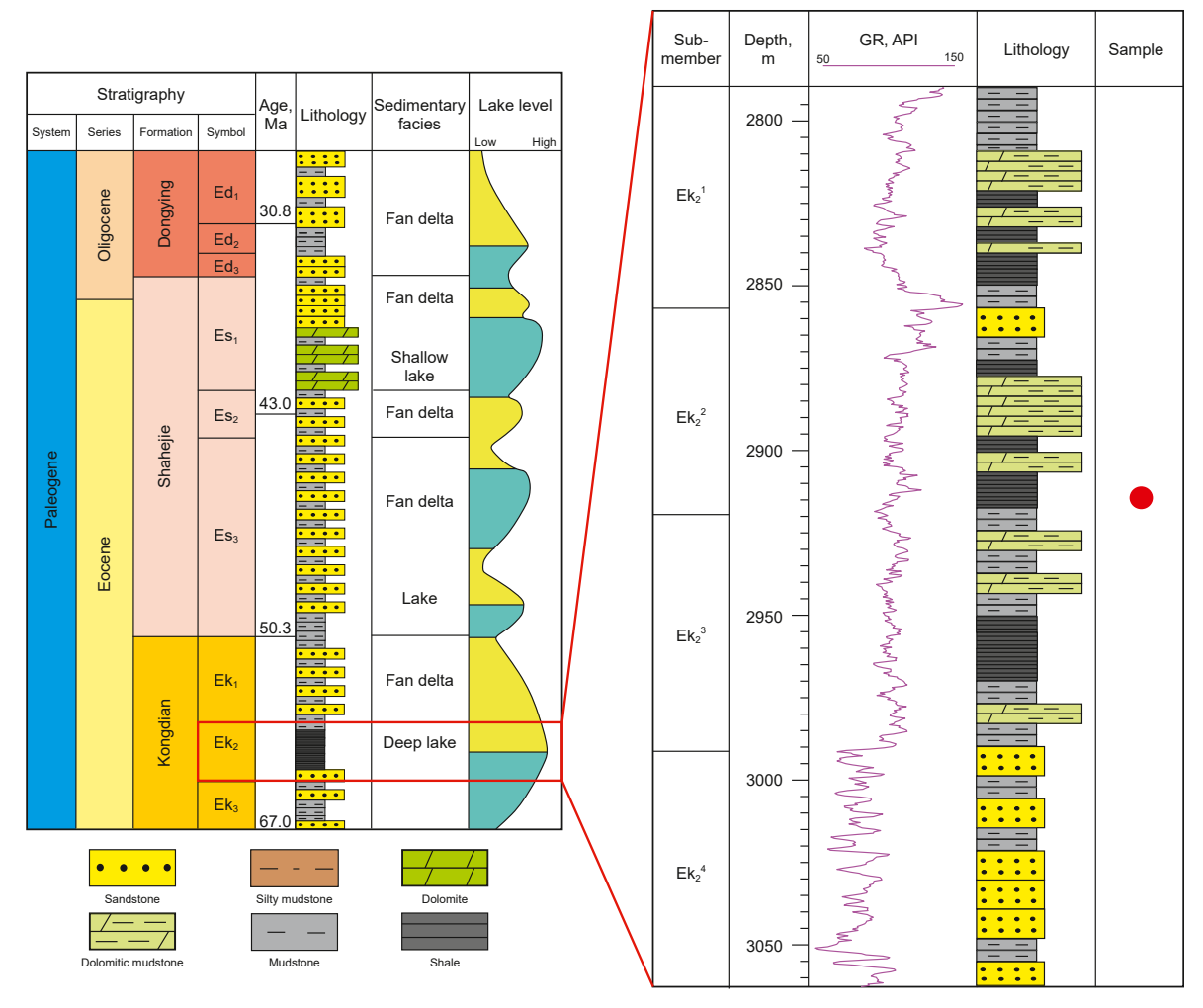
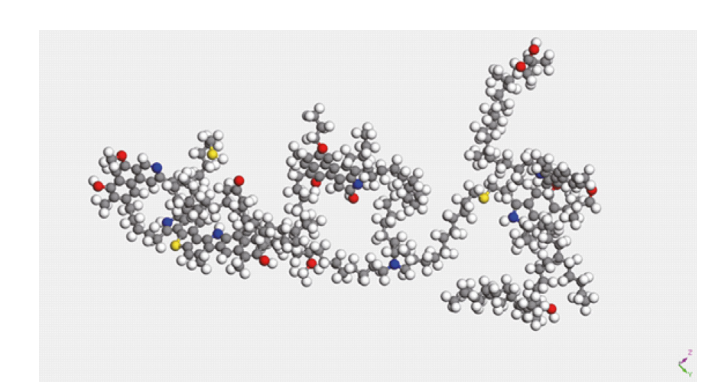


Fig. 2. Stratigraphic column and tectonic evolution of the Paleogene in Cangdong Sag (left). Lithologic column and sample distribution in the study interval (right).

**Table 1**Basic geochemical parameters of shale in the thermal simulation experiment.

Lithology	TOC, %	R <sub>o</sub> , %	Kerogen	$S_1$ , $mg \cdot g^{-1}$	$S_2$ , mg $\cdot$ g $^{-1}$	Clay, %	Quartz + feldspar, %	Calcite + dolomite, %	Other, %
Grey shale	7.87	0.55	I	1.28	60.94	27.0	22.0	17.0	34.0



**Fig. 3.** The molecular model unit of kerogen I-A at the immature stage. Color code: C (black), H (grey), O (red), N (blue), S (yellow).

complex systems (Van Duin et al., 2001). The overall energy of the system is composed of various components:

$$E_{\rm system} = E_{\rm bond} + E_{\rm over} + E_{\rm under} + E_{\rm val} + E_{\rm pen} + E_{\rm tors} + E_{\rm conj} + E_{\rm vdWaals} + E_{\rm Coulomb}$$
 (1)

#### 3.3.2. Simulation methods

The study showed the molecular dynamic simulations utilizing the large-scale atomic/molecular massively parallel simulator (LAMMPS) software (Liu et al., 2022). Firstly, the simulation system ran a low temperature molecular dynamic with minimal energy for 20 ps. After that, The ReaxFF force field parameters used in the simulations were obtained from the Reax package within the LAMMPS software (Zheng et al., 2017). The NVT ensemble with a time step of 0.25 fs was employed during the simulations, indicating no mass or heat transfer resistance between the simulation box and the external environment. The heat-up simulations were performed with a heating rate of 1 K/ps, spanning the temperature

range of 300–8000 K. For the isothermal pyrolysis simulations, a longer simulation time of 2 ns was employed at various temperatures ranging from 300 to 8000 K to investigate the effects in more detail. During the pyrolysis simulations, the volatiles (oil and gas) produced interacted with unreacted kerogen molecules within the simulation box and underwent additional reactions. In the isothermal simulations, an elevated temperature approach was implemented to observe thermolysis reactions over a realistic duration. To ensure the reliability of the pyrolysis process description, three parallel simulations were conducted for each set of simulation conditions. Periodic boundary conditions were applied in all directions to the cubic simulation box in all ReaxFF MD simulations.

#### 4. Results

#### 4.1. Main products distribution characteristics from experiments

Table 2 displays the results obtained from the thermal simulation experiment on the samples. The experiment revealed a gradual decrease in total organic carbon (TOC) content as the pyrolysis temperature increased, with TOC decreasing from 7.87% to 3.30%. The TOC that appears at a higher temperature point (>673.15 K) increases slightly. This increase is due to the reduction in shale quality caused by drainage and hydrocarbon expulsion, resulting in a relative increase in TOC content (Deng et al., 2021; Liu et al., 2022). The concentration of free hydrocarbon (S<sub>1</sub>) showed an initial increase from 300 to 648.15 K, followed by a decline after 648.15 K. Similarly, the pyrolysis monster (S<sub>2</sub>) displayed a declining trend with temperature, although the rate of decrease slowed down after 648.15 K (Fig. 4(a)).

In general, the gas products obtained from the simulation experiment involving hydrocarbon source rock production and emission comprised both hydrocarbon gases and inorganic gases such as CO<sub>2</sub>, H<sub>2</sub>, CO, and NH<sub>3</sub>. The gas production rate increased with the simulation temperature, with a particularly high rate observed in the oil production window. This suggests a strong correlation between gas production and oil production. The gas production rate continued to increase throughout the high-over maturity stage (Fig. 4(b)).

The hydrocarbon production rates for total oil and retained oil exhibited three distinct stages with increasing simulated temperature. Firstly, a slow growth stage of production rate (0.50%–0.75%) was observed as an early stage before reaching the peak of oil production. The second stage was characterized by a rapid increase

in the production rate (0.75%–1.20%), corresponding to the thermal evolution reaching its peak and the maximum hydrocarbon production rate at 0.80%. The retained oil reached its peak at  $R_{\rm o}=1.0$ % with the highest experimental yield, whereas the yields of total oil, total hydrocarbon, and retained oil showed the highest increase rate at  $R_{\rm o}=1.0$ % and subsequently reached a maximum at  $R_{\rm o}=1.2$ %. In the third stage, a rapid decrease in yield (1.20%–2.50%) was observed, with the yield of retained oil declining after  $R_{\rm o}=1.00$ %. The yields of total hydrocarbon, total oil, and discharged oil peaked at  $R_{\rm o}=1.20$ %, indicating an earlier peak in retained oil generation compared to discharged oil, total contained oil, and total hydrocarbon (Fig. 4(c)).

Analysis of the yields of retained oil, discharged oil, and total oil revealed a significant proximity between the temperature point where the yield of discharged oil exhibited the fastest increase and the temperature point where the yield of retained oil started to decline. Moreover, the trends in the yield of total oil and retained oil were found to be closely aligned, suggesting a correlation between the yield of retained oil and total oil.

#### 4.2. Molecular biomarkers characteristics of retained oil

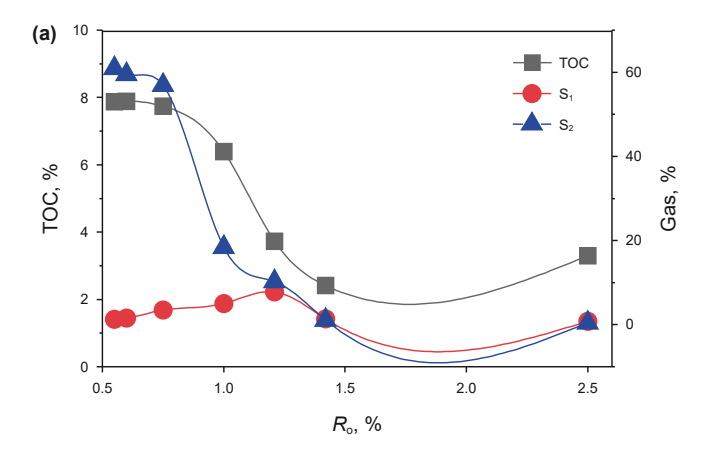
#### 4.2.1. Chromatographic characteristics of saturated hydrocarbons

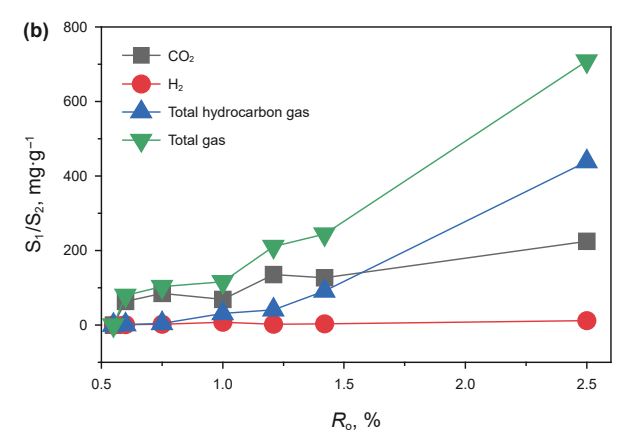
The carbon distribution of saturated hydrocarbons in the original sample ranged from  $nC_{14}$  to  $nC_{38}$ . Specifically,  $C_{23}$  was the predominant carbon peak with an OEP (odd-even predominance) value of 1.54, demonstrating a strong odd-even dominance. The OEP value is a parameter used to determine the maturity. The experimental results are summarized in Table 3, and the chromatograms showed variations in each temperature stage during the thermal simulation experiment (Fig. 5). The retained oil in the thermal simulation experiment contained n-alkanes ranging from  $C_{14}$  to  $C_{36}$ . The  $\sum nC_{21-} \sum nC_{22}+$  parameter indicated a dominance of high carbon number alkanes in the thermal simulation experiment, suggesting that heavier hydrocarbon components were more easily retained.

When the temperature in the thermal simulation experiment did not exceed 623.15 K, the chromatogram of the retained oil displayed a single-peak pattern, and the main peak carbon increased as the experimental temperature rose. However, after 673.15 K, a double-peak characteristic was observed, and the main peak carbon shifted backward. The OEP value of the retained oil obviously changes. The larger the value, the lower the maturity. The OEP value of 1.00–1.20 is mature organic matter, 1.20–1.40 is low-mature organic matter, and >1.40 is immature organic matter.

**Table 2**Organic geochemical characteristics and hydrocarbon products from the pyrolysis experiments of the shale samples.

Sample	: 1	Гетрегаt	ure, K	Formation press	sure, MPa Lithostatic pressure	, MPa R <sub>o,</sub> %	TOC, %	$S_1$ , $mg \cdot g^{-1}$	$S_2$ , mg·g $^{-1}$
G9-1		_		35	71	0.55	7.87	1.28	60.94
G9-2	5	573.15		35	71	0.60	7.89	1.61	59.52
G9-3	5	598.15		40	79	0.75	7.74	3.46	56.89
G9-4	6	523.15		47	94	1.00	6.39	5.04	18.36
G9-5	6	648.15		53	106	1.21	3.73	7.78	10.27
G9-6	6	573.15		58	116	1.42	2.41	1.34	1.11
G9-7	7	773.15		70	141	2.50	3.30	0.83	0.40
Sample	Total gas m <sup>3</sup> ·t <sup>-1</sup>				as, m <sup>3</sup> ·t <sup>-1</sup> Expelled liquid hydrocarbo	on, kg·t <sup>-1</sup> Retained	liquid hydrocarbo	on, kg·t <sup>-1</sup> Total hyd	rocarbon, kg·t <sup>-1</sup>
G9-1	0.00	0.00	0.00	0.00	0.00	0.00		0.00	
G9-2	79.04	63.17	1.49	1.09	5.41	65.79		35.49	
G9-3	103.00	85.10	1.69	4.28	14.02	153.07		171.97	
G9-4	116.35	69.24	7.24	31.50	38.17	500.46		568.04	
G9-5	211.09	135.91	2.09	41.01	449.49	281.58		783.44	
G9-6	243.98	126.79	2.76	91.47	382.15	54.08		558.03	
G9-7	708.11	224.32	11.65	438.51	189.46	6.26		590.66	





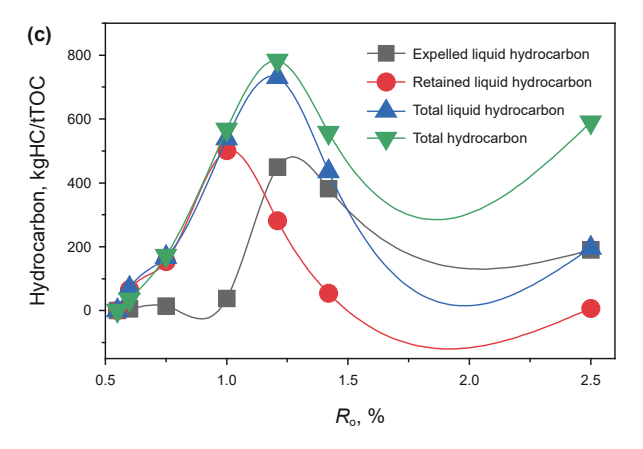


Fig. 4. Hydrocarbon generation rates of shale sample in thermal simulation.

**Table 3**Aliphatic hydrocarbon molecular composition characteristics of the retained hydrocarbons.

Temperature, K	Maximum peak	$\textstyle{\sum} nC_{21-}/{\sum} nC_{22} +$	OEP	Pr/nC <sub>17</sub>	Ph/nC <sub>18</sub>
573.15	C23	0.47	1.43	1.10	1.66
598.15	C23	0.51	1.29	0.95	0.87
623.15	C23	0.51	1.20	0.27	0.29
648.15	C21	0.61	1.02	0.11	0.08
673.15	C20	1.13	1.00	0.04	0.03
773.15	C22	0.74	1.01	0.08	0.14

Note: OEP=  $(nC_{21}+6 \times nC_{23}+nC_{25})/(4 \times nC_{22}+4 \times nC_{24})$ .

Moreover, the OEP value of retained oil was lower at higher temperatures of the thermal simulation experiment, but it did not show significant variations after 648.15 K.

# 4.2.2. Chromatographic mass spectrometric characterization of saturated hydrocarbons

Tricyclic terpene, gamma waxane, and patchouli were analyzed in the mass spectra of m/z 191 terpene chromatograms in the retained oil. The distribution of terpene series compounds in the retained oil showed similar trends, with patchouli having the highest content at 573.15 K, followed by gamma waxane. The content of gamma waxane decreased with increasing temperature in the thermal simulation experiment, and the same trend was observed for patchouli (Fig. 6).

In the m/z 217 sterane chromatogram, mass spectra revealed the presence of rule sterane, rearranged sterane, and other compounds. Fig. 7 illustrates that the relative contents of regular steranes  $C_{27}$ ,  $C_{28}$ , and  $C_{29}$  reached their lowest point at 648.15 K and then increased with temperature. Overall,  $C_{29}$  regular steranes dominated at all temperature points in the retained oil.

# 4.3. Main products distribution characteristics from molecular simulation

During the pyrolysis simulations, the volatiles (oil and gas) produced remained in the simulation box with the unreacted kerogen molecules and underwent additional reactions. Realistic simulation periods were observed using an elevated temperature technique to induce thermolysis reactions. In all ReaxFF MD simulations, periodic boundary conditions were applied to the cubic box in all directions.

In the first stage, the reactant  $(C_{40+})$  undergoes a preliminary reaction before 2000 K, and the reaction proceeds slowly. The second stage, known as the fast pyrolysis stage and the primary stage of pyrolysis reaction, was identified to occur between 2000 K and 5000 K. During this stage, the reactant  $(C_{40+})$  rapidly depleted, and stage III, the late stage of pyrolysis, appeared after 5000 K. The amount of  $C_{40}$  was extremely low at this point, but it began to slightly increase, signifying the start of coking (Fig. 8).

The first stage was characterized by a thermal breakdown reaction with a slow reaction rate. Slow growth in the heavy oil components ( $C_{16}$ – $C_{40}$ ) was observed. As the kerogen decreased,  $C_{16}$ – $C_{40}$  reached its maximum while the amount of  $C_5$ – $C_{15}$  dramatically increased. Stage III represented the final stage, where secondary cracking reactions predominated. This was indicated by the extremely low caseagen content, increased levels of gaseous chemicals ( $C_1$ – $C_4$ ), and inorganic compounds. The product distribution pattern revealed that the end of stage II could be the optimal time for oil production through pyrolysis, as the content of oil ( $C_5$ – $C_{15}$  and  $C_{16}$ – $C_{40}$ ) reached its maximum (Fig. 9).

For analysis, the retained oil content was analyzed at 4000 K, which represented the peak oil content. The evolution of organic gas indicated that the first molecule produced was  $C_2-C_5$ , followed by  $CH_4$  (Fig. 10(a)). The amounts of  $C_2-C_5$  and  $CH_4$  rapidly increased and became the main components of the gas. Additionally, the amount of  $C_2H_2$  continuously increased during the final stage of pyrolysis, suggesting a severe dehydrogenation reaction occurred, resulting in an increase in  $H_2$ .

Fig. 10(b) illustrates the trends in the yields of the three types of retained oil with temperature. These three types are categorized as  $C_{12}-C_{17}$ ,  $C_{18}-C_{23}$ , and  $C_{24}-C_{32}$ . All three types of retained oil showed an initial increase at the beginning of the reaction, although the rate of increase was relatively slow. The growth rate of  $C_{12}-C_{17}$  and  $C_{24}-C_{32}$  exceeded that of  $C_{18}-C_{23}$  since the decomposition reaction of organic matter produced oil and gas as the temperature increased. This allowed for the adsorption of its own kerogen first, followed by transport. The main reason for this result

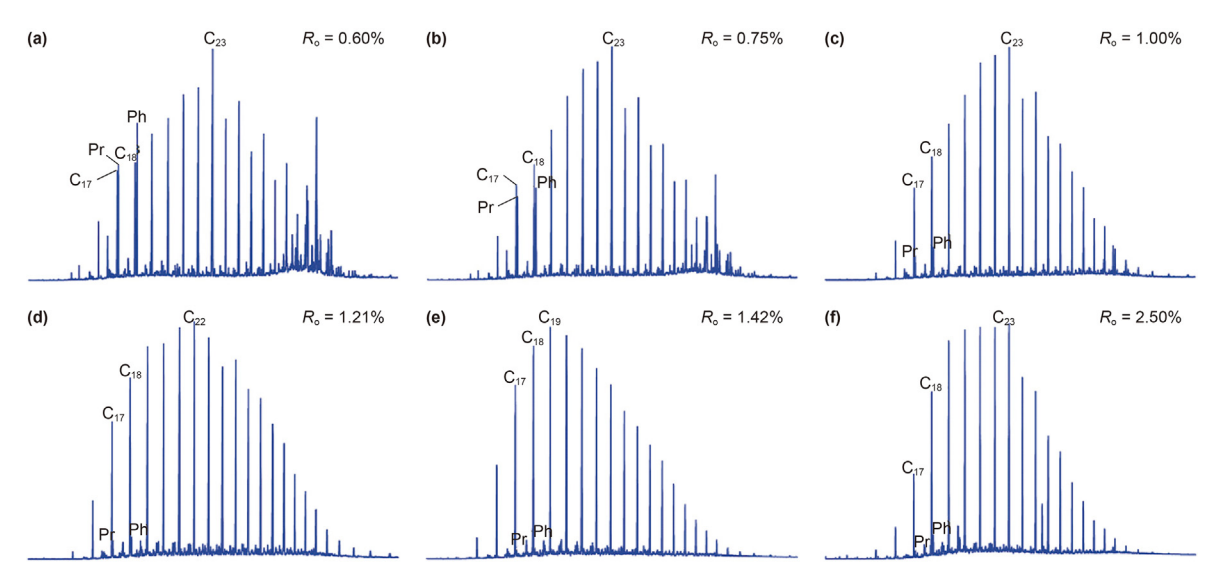


Fig. 5. N-alkane and isoprenoid distributions of retained hydrocarbons generated during the pyrolysis experiments.

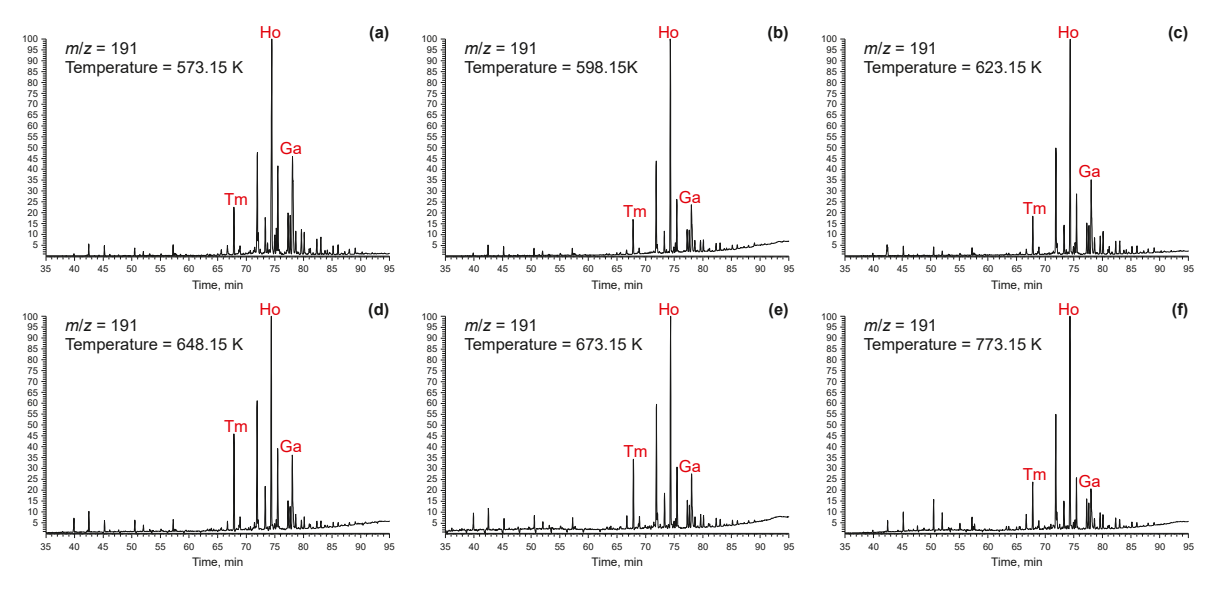


Fig. 6. Mass spectra of terpenes for retained oil.

is the further fracture reactions of macromolecules during later pyrolysis, which produce  $C_{12}$ – $C_{17}$  and  $C_{24}$ – $C_{32}$ . The organic matter in the oil shale was directly converted into free oil and adsorbed oil after the thermal decomposition reaction without going through an intermediate stage, or the adsorbed oil at this temperature cannot stabilize.

The change in the mass percentage of pyrolysis products quantitatively indicates the degree of reaction. When considering  $C_{33}-C_{40}$  as heavy oil, all the products increased as the reaction proceeded, and there was still kerogen fragments present. Furthermore, the cracking reaction was not fully complete, although the content of  $C_{33}-C_{40}$  was relatively small (Fig. 10(c)).

A significant number of gaseous byproducts and hydrocarbons were generated. Fig. 3 depicts the temporal history of these products. As shown in Fig. 10(d), the main inorganic gases produced included H<sub>2</sub>, H<sub>2</sub>S, and CO<sub>2</sub>. Specifically, the amounts of H<sub>2</sub>S and CO<sub>2</sub> increased with temperature, although the concentration of CO<sub>2</sub> remained relatively low and was primarily regulated by the quantity of carboxyl groups. The amount of hydrogen significantly

decreased after hydrogen synthesis, particularly at the third step. It can serve as a source of hydrogen energy. The low concentration of  $H_2S$  was primarily due to the absence of thiol groups and favorable interactions with other radicals at high temperatures. The high temperature and low CO concentration were identified due to the amount of  $CO_2$  and the simulation parameters.

#### 5. Discussions

# 5.1. The comparation between pyrolysis simulation experiment with molecular simulation

In this study, molecular dynamics simulation and thermal simulation experiments were used to study the evolution characteristics of retained oil. The molecular simulation and experimental results will be analyzed and explained below.

Through the comparison of the results, it can be seen that the molecular simulation results of the reactants are generally consistent with the variation trends of the simulation experiment results,

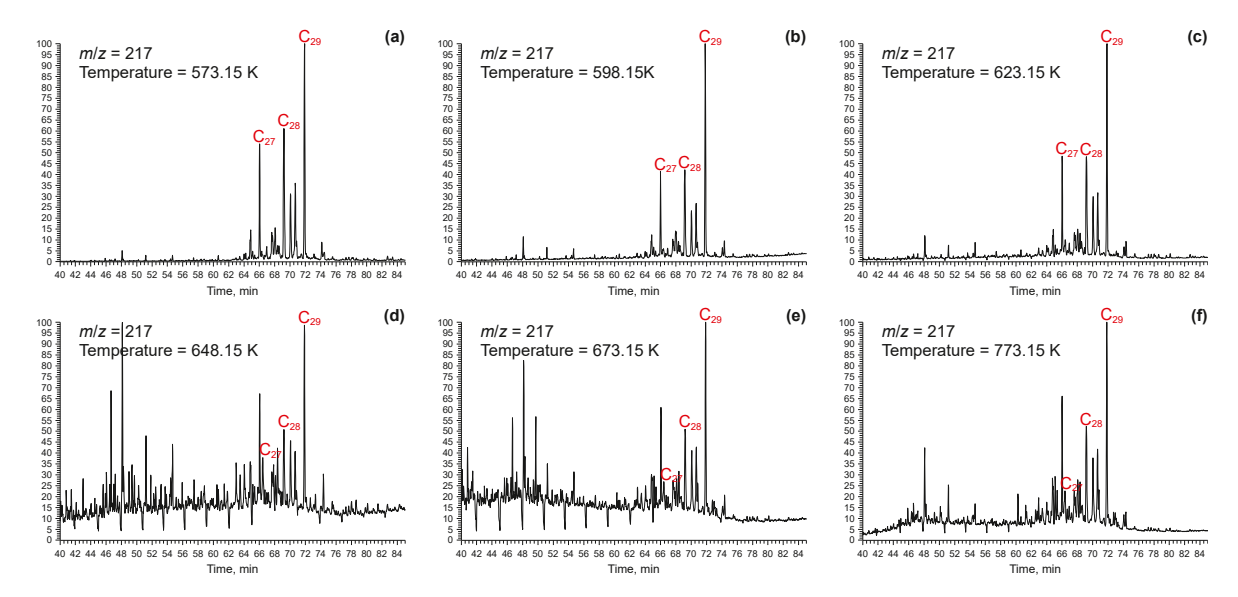


Fig. 7. Mass spectra of steranes for expelled and retained oil.

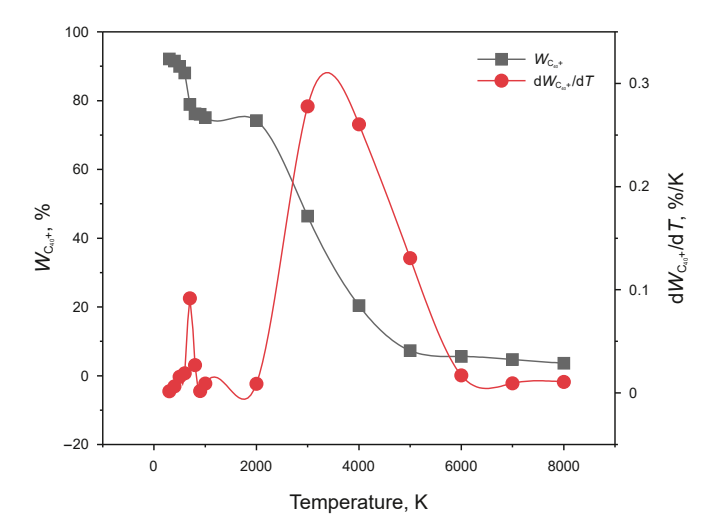


Fig. 8. The weight loss curves of  $C_{40+}$  compounds during ReaxFF MD simulations.

but there are also differences.

The consistency is manifested in two aspects: first, the experimental results of the two methods can be divided into three stages, and the three stages are slow reduction, rapid reduction and gradual stabilization, indicating that the overall evolution trend of the reactants is consistent; secondly, the change characteristics of the reactants of the two analytical methods and experimental methods are similar, and the reactions of the reactants in the two methods are all carried out thoroughly (Fig. 11).

The difference is mainly reflected in the difference at the critical moment of reactant change, which is mainly due to the different experimental conditions of the two pyrolysis simulation experiments capture reactions occurring over short time scales. However, molecular simulations can capture reactions at an even finer time resolution, providing detailed insights into retention evaluation.

Through the comparison of the results, it can be seen that there is a certain deviation between the molecular simulation and the physical experiment data, but the difference is small. The main reason is that the difference in test methods has affected the results to a certain extent. Comparing the molecular simulation and

experimental test results shows that the overall evolution trend is consistent, and the difference is small. Therefore, the data is still very credible overall.

#### 5.2. The contents of retained oil evolution characteristics

The results from the thermal simulation experiments demonstrated a consistent trend with the molecular simulation results. Initially, the hysteretic oil content increased during the early stages of the pyrolysis reaction and then gradually decreased. This similarity between the two sets of results indicates that the molecular simulation findings largely represented the outcomes of the experimental analysis.

During the first stage of lag oil production, there was a significant increase in the yield of lag oil. The samples underwent rapid oil generation while excluding hydrocarbons, reaching the peak of hydrocarbon generation. The second stage saw a decline in the yield, suggesting a decrease in the efficiency of lag oil production. In the third stage, lag oil production showed low efficiency, with an emphasis on cracked gas generation (Fig. 12(a)).

The molecular simulation results revealed that both  $C_5-C_{15}$  and  $C_{16}-C_{40}$  compounds exhibited a similar trend of initially increasing and then decreasing. The rate of product change also varied considerably (Fig. 12(b)). The continuous increase of  $C_5-C_{15}$  and  $C_{16}-C_{40}$  indicated that higher temperatures facilitated the generation of short-chain compounds, thereby increasing the production of these components. However, their content decreased as the temperature increased, indicating that higher temperatures promoted the cleavage of  $C_{40+}$  compounds. Some of these  $C_{40+}$  compounds were not completely formed through direct pyrolysis reactions but instead experienced repeated decomposition and polymerization. This suggests that when the temperature surpassed a certain threshold, pure kerogen underwent a polymerization reaction at high temperatures to produce  $C_{40+}$ .

The characteristics of the three types of retained oil, namely  $C_{12}-C_{17}$ ,  $C_{18}-C_{23}$ , and  $C_{24}-C_{32}$ , exhibited significant variations. The content of both  $C_{12}-C_{17}$  and  $C_{18}-C_{23}$  continuously increased (Fig. 12(c)), with a much greater increase observed for movable oil and its rate of product change. In contrast, the content of  $C_{18}-C_{23}$  exhibited a slower increase. Throughout the pyrolysis process, the content of  $C_{12}-C_{17}$  continued to rise, albeit with changes in the rate

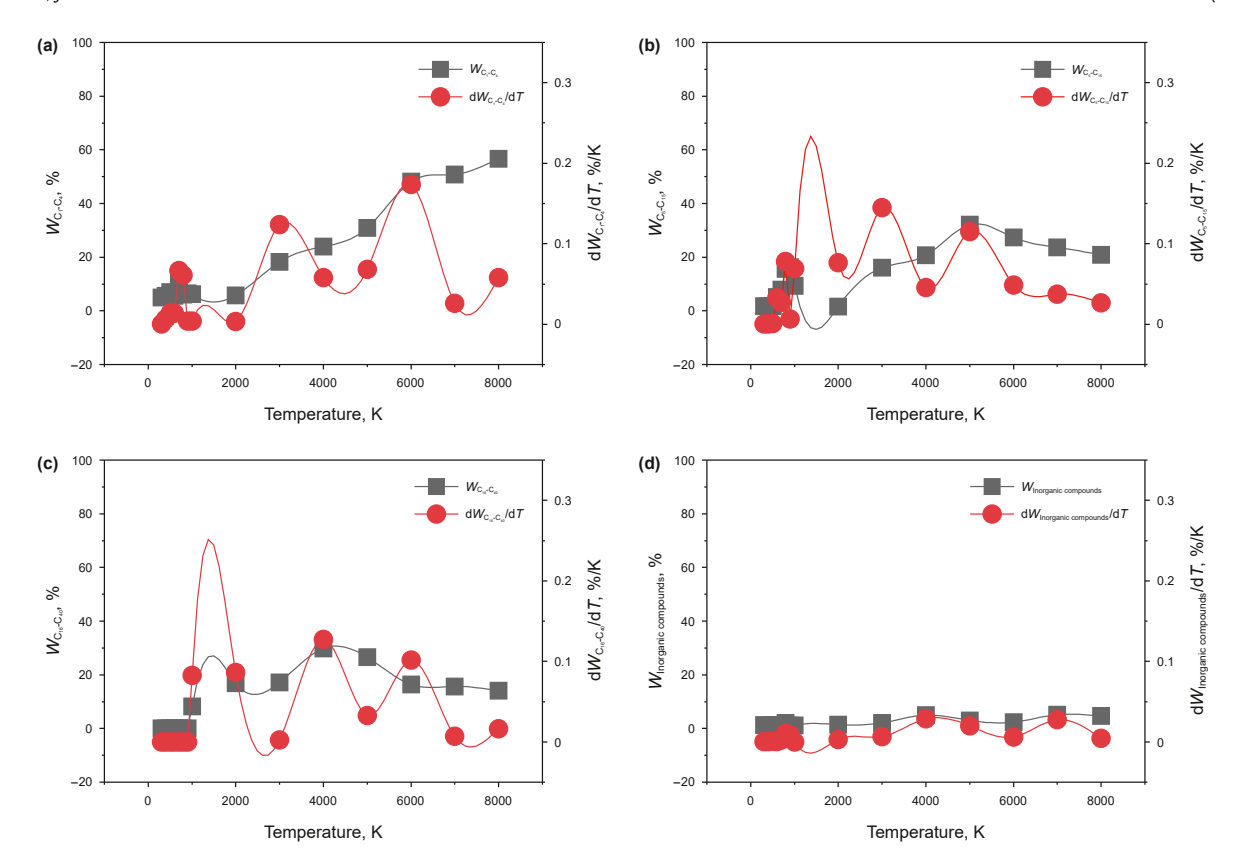


Fig. 9. The distribution of decomposition products from 300 K to 8000 K. (a)  $C_1-C_4$ ; (b)  $C_5-C_{15}$ ; (c)  $C_{16}-C_{40}$ ; (d) inorganic compound.

of product change. Specifically, the early stage of production was directly generated from the pyrolysis of kerogen, while the later stage was primarily a result of secondary cleavage. The stability of long-chain macromolecules decreased, leading to the generation of smaller chain hydrocarbon molecules and so on. On the other hand, the content of C<sub>18</sub>-C<sub>23</sub> remained unchanged during the late stage of pyrolysis. These results indicate that a dynamic equilibrium was reached at the late stage, with the peak being reached at 5000 K. Subsequently, the content of components no longer changed as the reaction progressed. This suggests that the bound shale oil reached a steady state when the upper limit of binding was reached. The amount of C<sub>24</sub>-C<sub>32</sub> retained oil tended to increase (Fig. 12(d)), with its growth occurring in two stages. The initial increase was due to the oil produced from the pyrolysis of kerogen, which was subsequently adsorbed by the reservoir. Its content no longer increased once the upper limit of adsorption was reached. The second increase was attributed to the significant amount of adsorbed oil generated as the pyrolysis reaction progressed, leading to an elevated yield of adsorbed oil.

#### 5.3. Generation mechanism of retained oil

Cheesecake roots are complex polymers composed of carbon, hydrogen, oxygen, nitrogen, and sulfur, cross-linked with aliphatic, aromatic, and heterogeneous atoms. During the pyrolysis process, the covalent bonds of kerogen gradually break, forming free radicals that generate oil, gas, and residual coke through cleavage, cross-linking, and condensation processes (Amer et al., 2022; Loron et al., 2022).

Based on comprehensive analysis (Fig. 13), the sequence of bond breaking in different stages is elucidated as follows. In the first stage, as the temperature gradually increases, the macromolecule begins to break, and hot pitch is generated. The amount of hot pitch increases with pyrolysis temperature, as bridging bonds break to form free radicals or unsaturated bonds, resulting in the generation of shale oil and dry distillation gas. Also, ether bonds break to form hydroxyl groups, which de-functionalize to generate  $H_2O$ . The carboxyl group yields  $CO_2$ , and the C-N bond of acid amide cleaves to synthesize  $NH_3$  at this stage. These bonds have relatively small bond energy.

In the second stage, the yield of retained oil increases rapidly until reaching a maximum. As the temperature further rises, the yield of retained oil begins to decline. The side chains of aromatic rings break, generating alkanes and olefins with different carbon numbers. Notably, the breaking effect is significant at the  $\beta$ -position connected to an aromatic carbon atom, as the conjugated double bond affects the strength of adjacent chemical bonds. Thus, the bond level at the  $\alpha$ -position increases, while the bond level at the  $\beta$ -position decreases. The bond orders of these broken bonds have higher values, between 0.7 and 0.9, with relatively lower bond energy. In stage II, the bond orders of these broken bonds range between 0.9 and 1.0, in line with previous research (Borrego et al., 2000; You et al., 2019; Liu et al., 2023), and the corresponding bond dissociation energies (BDEs) of representative bonds are shown in Fig. 14.

In the third stage, the hot asphalt is almost completely decomposed. The side chains of cycloalkanes break to form cycloalkane structures. Subsequently, ring structures undergo ring-opening reactions to synthesize paraffins and free radicals. The further cleavage of aliphatic chains leads to the production of small gases. Additionally, cyclic alkenes undergo partial secondary polycondensation and dehydrogenation, forming more stable aromatic rings.

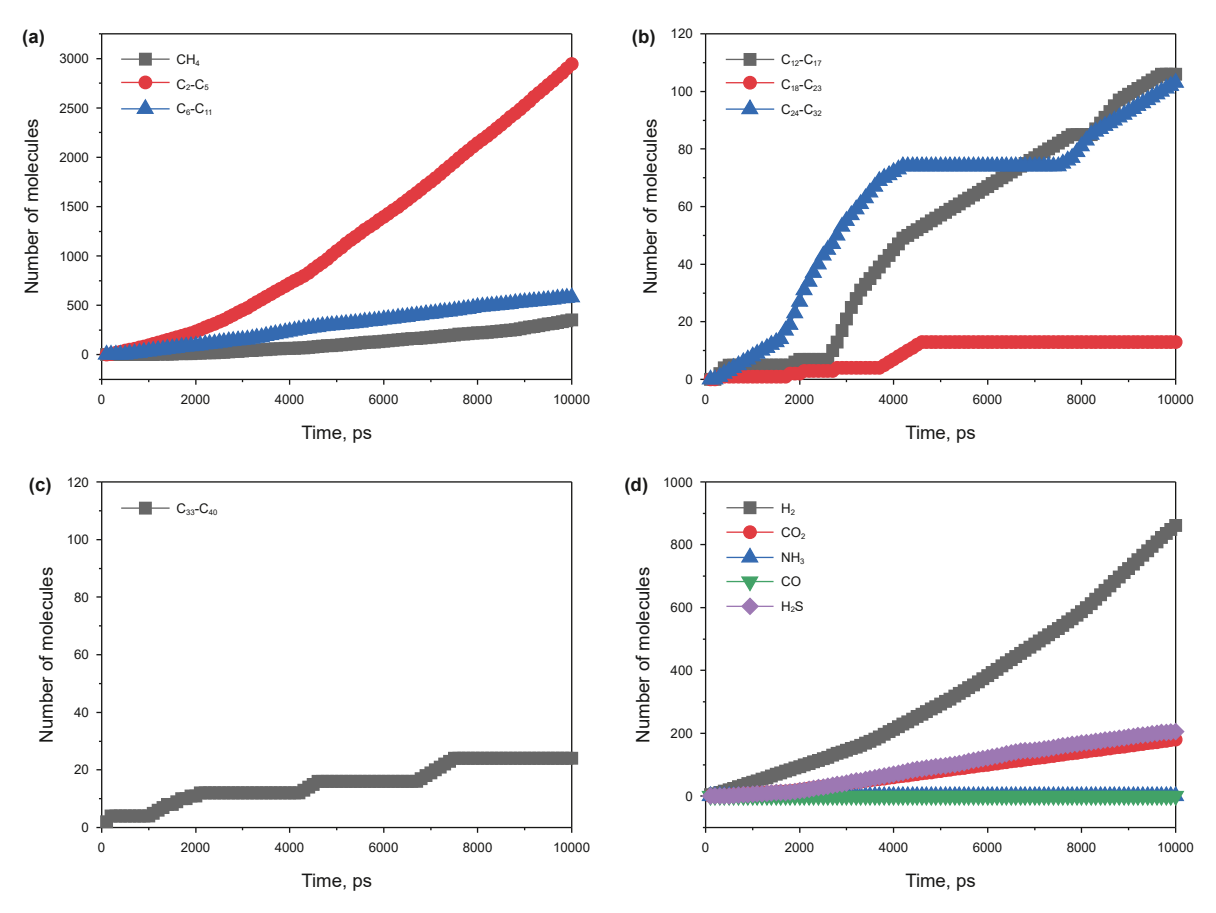


Fig. 10. The distribution of products during the pyrolysis of the kerogen at 4000 K.

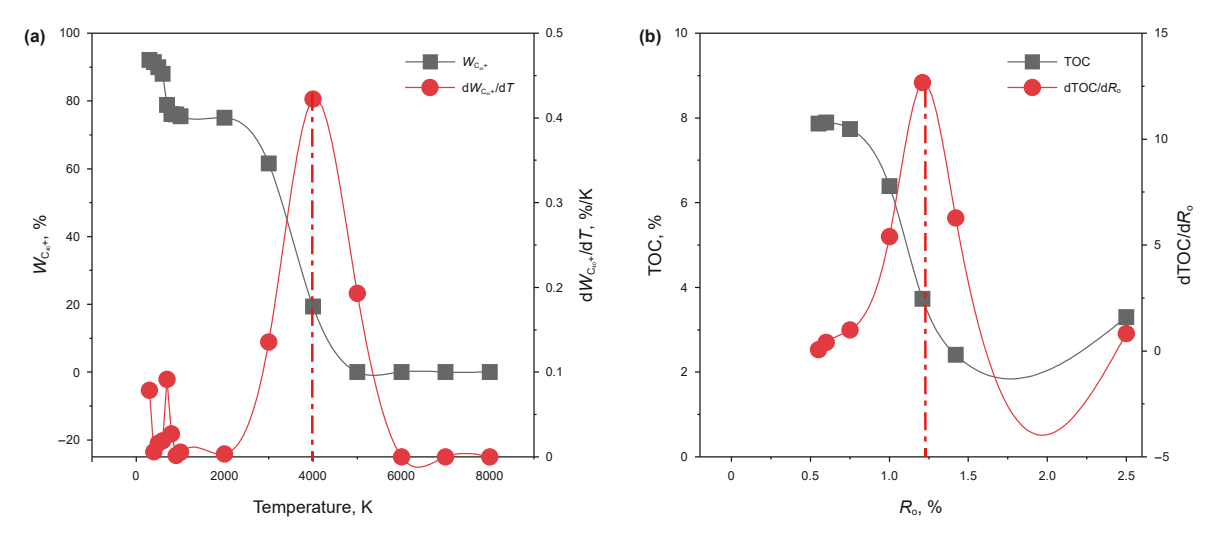


Fig. 11. The weight loss curves of C<sub>40+</sub> compounds during ReaxFF MD simulations (a) and the experimental results of TOC are shown in (b).

#### 6. Conclusions

The retained oil yield of the lake phase shale exhibited an increasing and then decreasing trend with increasing thermal simulation temperature, peaking at  $T=623.15~\rm K~(R_0=1.00\%)$ . The trend of retained oil yield observed in the thermal simulation experiments was consistent with the results obtained from ReaxFF MD, although there was a difference in the peak of retained oil yield. The production of retained oil during the pyrolysis process

can be divided into three stages. Stage I (300–2000 K) corresponds to the initial pyrolysis stage, characterized by a slow reaction rate and thermal decomposition of the reactants ( $C_{40+}$ ). Stage II (2000–5000 K) represents the fast pyrolysis stage and the main reaction stage, where the yield of retained oil increases rapidly. Stage III corresponds to the late stage of pyrolysis, with  $C_{40+}$  initially being very low and then increasing, indicating a transition in product evolution from decomposition to cross-linking reactions. The formation of retained oil involves three stages. In the first stage,

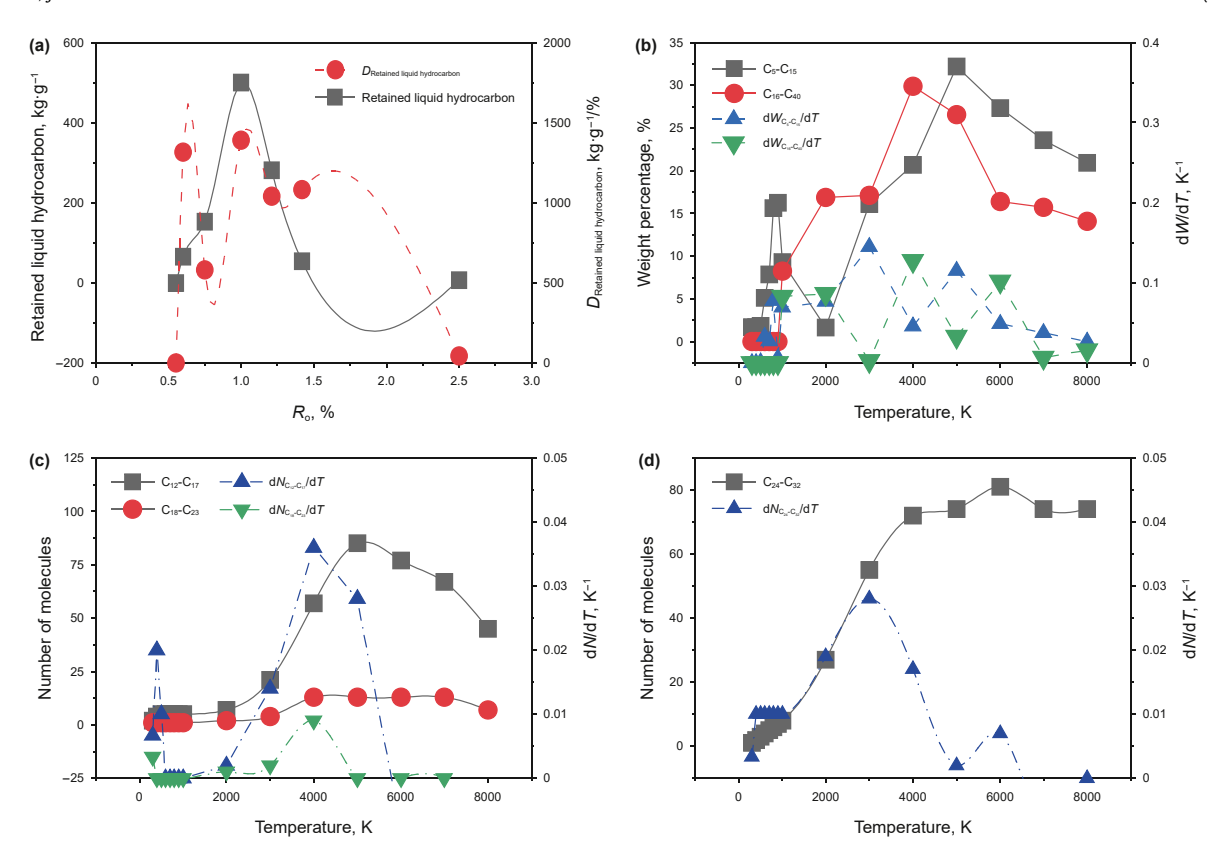


Fig. 12. The distribution of retained oil from experiments (a) and different types (b)  $C_5 - C_{40}$ ; (c)  $C_{12} - C_{17}$ ,  $C_{18} - C_{23}$ ; (d)  $C_{24} - C_{32}$ .

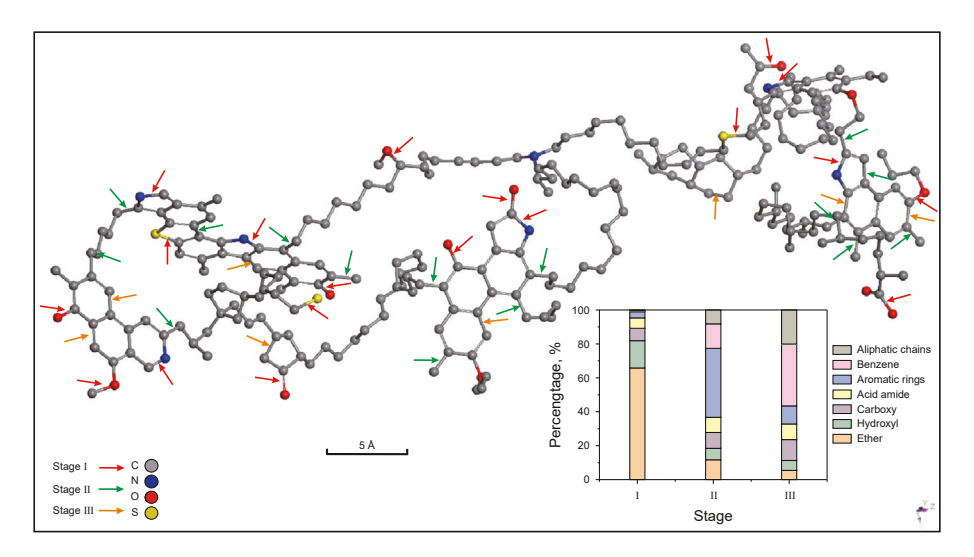


Fig. 13. Statistical results of bond breaking sites and the bond order of kerogen model in different stage.

weak bonds such as bridging bonds (hydroxyl, oxy, peroxy, imino, amino, and nitro), ether bonds, and acid amides begin to break, forming macromolecular intermediates and a minor amount of gas. The second stage involves the breaking of aromatic ring structures and the carbon chains of heteroatomic functional groups. Lastly, in the third stage, ring-opening reactions occur, resulting in the generation of short-chain olefins and radicals from the ring structures, as well as further breaking of aliphatic chains.

### **CRediT authorship contribution statement**

**Biao Sun:** Writing — original draft, Resources, Methodology, Investigation, Formal analysis. **Xiao-Ping Liu:** Writing — review & editing, Resources, Funding acquisition. **Jie Liu:** Supervision, Investigation, Formal analysis. **Tian Liu:** Visualization, Validation, Software, Methodology. **Zu-Xian Hua:** Visualization, Validation, Resources, Methodology. **Wen-Di Peng:** Validation, Methodology, Conceptualization.

Stage	Representative breaking bonds and their corresponding BDEs					
I		R O R R ~50 kcal/mol				
П	R R ~61 kcal/mol	R R R R R R R R R R R R R R R R R R R	NH <sub>2</sub> NH NH NH NH NH			
III	HO R R ~75 kcal/mol	R HS R ~76 kcal/mol	R R R			

Fig. 14. Representative breaking bonds and their corresponding BDEs. The BDE values (orange) are taken from Meuwly et al. (2002) and Liu et al. (2015); and the red dashed lines indicated the breaking bonds.

#### **Declaration of competing interest**

The authors declare that they have no known competing financial interests or personal relationships that could have appeared to influence the work reported in this paper.

#### Acknowledgments

This work was financially supported by the National Natural Science Foundation of China (Grant No. 42072150) and we thank the sponsors of these projects.

#### References

Al, Areeqi S., Bahamon, D., Polychronopoulou, K., Vega, L.F., 2022. Insights into the thermal stability and conversion of carbon-based materials by using ReaxFF reactive force field: recent advances and future directions. Carbon 196 (5), 840–866. https://doi.org/10.1016/j.carbon.2022.05.035.

Amer, M.W., Aljariri Alhesan, J.S., Marshall, M., Fei, Y., Roy Jackson, W., Chaffee, A.L., 2022. Comparison between reaction products obtained from the pyrolysis of marine and lacustrine kerogens. Fuel 337, 126839. https://doi.org/10.1016/ j.fuel.2022.126839.

Amine, Ifticene M., Yuan, C., Al-Muntaser, A.A., Onishchenko, Y.V., Emelianov, D.A., Varfolomeev, M.A., 2022. Behavior and kinetics of the conversion/combustion of oil shale and its components under air condition. Fuel 324, 124597. https:// doi.org/10.1016/j.fuel.2022.124597.

Arvelos, S., Abrahão, O., Eponina Hori, C., 2019. ReaxFF molecular dynamics study on the pyrolysis process of cyclohexanone. J. Anal. Appl. Pyrol. 141, 104620. https://doi.org/10.1016/j.jaap.2019.05.009.

Barnie, S., Zhang, J., Duncan, A.E., Osei-Marfo, M., Adenutsi, C.D., Chen, H., 2022. The adsorption and reduction mechanism of Cr(VI) by kerogen with different degrees of geochemical alteration using a thermal simulation method. Appl. Geochem. 140, 105261. https://doi.org/10.1016/j.apgeochem.2022.105261.

Borrego, A.G., Prado, J.G., Fuente, E., Guillén, M.D., Blanco, C.G., 2000. Pyrolytic behaviour of Spanish oil shales and their kerogens. J. Anal. Appl. Pyrol. 56 (1), 1–21. https://doi.org/10.1016/S0165-2370(99)00092-3.

Castro-Marcano, F., Russo, M.F., Van Duin, A.C.T., Mathews, J.P., 2014. Pyrolysis of a large-scale molecular model for Illinois no. 6 coal using the ReaxFF reactive force field. J. Anal. Appl. Pyrol. 109 (6), 79–89. https://doi.org/10.1016/ij.aap.2014.07.011.

Deng, M., Zhai, C.B., Yang, Z.H., Duan, X.G., Zheng, L.J., Song, Z.X., 2021. Thermal simulation experiment on hydrocarbon generation characteristics of lowmature marine black shale. Sci. Technol. Eng. (1), 130–137 (in Chinese). http://isvgc/article/abstract/1913229.

Dong, Q.-Y., Liu, X., Li, H.-X., Liu, Z.-C., Liu, Q.-X., Dong, Q., 2013. Formation conditions of shale oil reservoir in the second Member of Kongdian Formation in

southern Kongdian area, Huanghua depression. Nat. Gas Geosci. 24 (1), 188–198. https://doi.org/10.11764/j.issn.1672-1926.2013.01.188.

Dunkel, C.A., Vázquez-Ortega, A., Evans, J.E., 2022. Black shale—gray shale transitions in a Late Devonian shale succession, Central Appalachian Basin (Northern Ohio): sedimentary and geochemical evidence for terrestrial organic matter input driving anoxia events. Palaeogeogr. Palaeoclimatol. Palaeoecol. 608, 111271. https://doi.org/10.1016/j.palaeo.2022.111271.

Fu, J., Li, S., Niu, X., Deng, X., Zhou, X., 2020. Geological characteristics and exploration of shale oil in chang 7 member of triassic yanchang formation, Ordos Basin, NW China. Petrol. Explor. Dev. 47 (5), 931–945. https://doi.org/10.1016/S1876-3804(20)60107-0.

Goodarzi, F., 2020. Comparison of the geochemistry of lacustrine oil shales of mississippian age from nova scotia and new brunswick, Canada. Int. J. Coal Geol. 220, 103398. https://doi.org/10.1016/j.coal.2020.103398.

Hail, Hakimi M., Lotfy, N.M., El Nady, M.M., Makled, W.A., Ramadan, F.S., Rahim, A., 2023. Characterization of lower cretaceous organic-rich shales from the kom ombo basin, Egypt: implications for conventional oil generation. J. Asian Earth Sci. 241, 105459. https://doi.org/10.1016/j.jseaes.2022.105459.

Horsfield, B., Mahlstedt, N., Weniger, P., Misch, D., Vranjes-Wessely, S., Han, S., 2022. Molecular hydrogen from organic sources in the deep Songliao Basin, P.R. China. Int. J. Hydrogen Energy 47 (38), 16750–16774. https://doi.org/10.1016/j.ijhydene.2022.02.208.

Hou, L.H., Luo, X., Lin, S.H., Li, Y.X., Zhang, L.J., Ma, W.J., 2022. Assessment of recoverable oil and gas resources by in-situ conversion of shale—case study of extracting the Chang 73 shale in the Ordos Basin. Petrol. Sci. 19 (2), 441–458. https://doi.org/10.1016/j.petsci.2021.10.015.

Jin, Z., Liang, X., Bai, Z., 2022. Exploration breakthrough and its significance of Gulong lacustrine shale oil in the Songliao Basin, Northeastern China. Energy Geoscience 3 (2), 120–125. https://doi.org/10.1016/j.engeos.2022.01.005.

Jin, Z., Nie, H., Liu, Q., Zhao, J., Jiang, T., 2018. Source and seal coupling mechanism for shale gas enrichment in upper ordovician wufeng formation - lower silurian longmaxi Formation in sichuan Basin and its periphery. Mar. Petrol. Geol. 97 (5), 78–93. https://doi.org/10.1016/j.marpetgeo.2018.06.009.

Jin, Z., Zhu, R., Liang, X., Shen, Y., 2021. Several issues worthy of attention in current lacustrine shale oil exploration and development. Petrol. Explor. Dev. 48 (6), 1471–1484. https://doi.org/10.1016/S1876-3804(21)60303-8.

Li, M., Chen, Z., Ma, X., Cao, T., Qian, M., Jiang, Q., 2019. Shale oil resource potential and oil mobility characteristics of the eocene-oligocene Shahejie Formation, jiyang super-depression, Bohai Bay Basin of China. Int. J. Coal Geol. 204, 130–143. https://doi.org/10.1016/j.coal.2019.01.013.

Li, W., Stevens, L.A., Zhang, B., Zheng, D., Snape, C.E., 2022a. Combining molecular simulation and experiment to prove micropore distribution controls methane adsorption in kerogens. Int. J. Coal Geol. 261, 104092. https://doi.org/10.1016/ icoal 2022 104092

Li, Y., Zhao, Q., Lyu, Q., Xue, Z., Cao, X., Liu, Z., 2022b. Evaluation technology and practice of continental shale oil development in China. Petrol. Explor. Dev. 49 (5), 1098–1109. https://doi.org/10.1016/S1876-3804(22)60335-5.

Li, M., Wang, M., Zhang, L., Wang, Q., Wang, X., Li, X., 2024. Understanding pore space and oil content of liquid-rich shale in the southern Bohai Sea, China. Geoenergy Science and Engineering 233, 212552. https://doi.org/10.1016/

j.geoen.2023.212552.

- Liu, X., Zhan, J.H., Lai, D., Liu, X., Zhang, Z., Xu, G., 2015. Initial pyrolysis mechanism of oil shale kerogen with reactive molecular dynamics simulation. Energy Fuel. 29 (5), 2987–2997.
- Liu, X., Lai, J., Fan, X., Shu, H., Wang, G., Ma, X., 2020. Insights in the pore structure, fluid mobility and oiliness in oil shales of Paleogene Funing Formation in Subei Basin, China. Mar. Petrol. Geol. 114, 104228. https://doi.org/10.1016/j.marpetgeo.2020.104228.
- Liu, J., Yang, Y., Sun, S., Yao, J., Kou, J., 2022a. Flow behaviors of shale oil in kerogen slit by molecular dynamics simulation. Chem. Eng. J. 434, 134682. https:// doi.org/10.1016/j.cej.2022.134682.
- Liu, X.P., Guan, M., Jin, Z.J., Cao, Z., Lai, J., Zheng, L.J., 2022b. Pore structure evolution of lacustrine organic-rich shale from the second member of the Kongdian formation in the Cangdong Sag, Bohai Bay Basin, China. Petrol. Sci. 19 (2), 459–471. https://doi.org/10.1016/i.petsci.2021.12.010.
- Liu, X.Y., Wu, K., Kong, Q.F., Liu, D.Y., Shi, J.F., Peng, P.G., 2022c. Semi-closed heat simulation experiment of a chang 7 member shale in the Ordos Basin. Geochimica 51 (4), 434–440. https://doi.org/10.19700/j.0379-1726.2022.04.006.
- Liu, S., Wei, L., Zhou, Q., Yang, T., Li, S., Zhou, Q., 2023. Simulation strategies for ReaxFF molecular dynamics in coal pyrolysis applications: a review. J. Anal. Appl. Pyrol. 170, 105882. https://doi.org/10.1016/j.jaap.2023.105882.
- Loron, C.C., Sforna, M.C., Borondics, F., Sandt, C., Javaux, E.J., 2022. Synchrotron FTIR investigations of kerogen from Proterozoic organic-walled eukaryotic microfossils. Vib. Spectrosc. 123, 103476. https://doi.org/10.1016/j.vibspec.2022.103476.
- Ma, Z., Tan, J., Zheng, L., Ni, C., Hu, R., Ma, J., 2022. Simulation experiment of fluid-feldspar sandstone interactions and their implications for tight oil and gas exploration of the Yanchang Formation, Ordos Basin, China. Mar. Petrol. Geol. 142, 1–33. https://doi.org/10.1016/j.marpetgeo.2022.105737.
- Meuwly, M., Becker, O.M., Stote, R., Karplus, M., 2002. NO rebinding to myoglobin: a reactive molecular dynamics study. Biophys. Chem. 98 (1–2), 183–207. https:// doi.org/10.1016/S0301-4622(02)00093-5.
- Olariu, C., Zhang, Z., Zhou, C., Yuan, X., Steel, R., Chen, S., 2022. Conglomerate to mudstone lacustrine cycles revealed in Junggar Basin, northwest China: middle permian lucaogou and jingjingzigou formations. Mar. Petrol. Geol. 136, 105473. https://doi.org/10.1016/j.marpetgeo.2021.105473.
- Omari, A., Wang, C., Li, Y., Xu, X., 2022. The progress of enhanced gas recovery (EGR) in shale gas reservoirs: a review of theory, experiments, and simulations. J. Petrol. Sci. Eng. 213, 110461. https://doi.org/10.1016/j.petrol.2022.110461.
- Pu, X., Zhou, L., Han, W., Zhou, J., Wang, W., Zhang, W., 2016. Geologic features of fine-grained facies sedimentation and tight oil exploration: a case from the second Member of Paleogene Kongdian Formation of Cangdong sag, Bohai Bay Basin. Petrol. Explor. Dev. 43 (1), 26–35. https://doi.org/10.1016/S1876-3804(16)30003-9.
- Saif, T., Lin, Q., Butcher, AR., Bijeljic, B., Blunt, MJ., 2017. Multi-scale multidimensional microstructure imaging of oil shale pyrolysis using X-ray microtomography, automated ultra-high resolution SEM, MAPS Mineralogy and FIB-SEM. Applied Energy 202, 628–47.
- Salmon, E., van Duin, A.C.T., Lorant, F., Marquaire, P.M., Goddard, Wa, 2009a. Early maturation processes in coal. Part 2: reactive dynamics simulations using the ReaxFF reactive force field on Morwell Brown coal structures. Org. Geochem. 40 (12), 1195–1209. https://doi.org/10.1016/j.orggeochem.2009.09.001.
- Salmon, E., van Duin, A.C.T., Lorant, F., Marquaire, P.M., Goddard, W.A., 2009b.

- Thermal decomposition process in algaenan of Botryococcus braunii race L. Part 2: molecular dynamics simulations using the ReaxFF reactive force field. Org. Geochem. 40 (3), 416–427. https://doi.org/10.1016/j.orggeochem.2008.08.012.
- Ungerer, P., Collell, J., Yiannourakou, M., 2015. Molecular modeling of the volumetric and thermodynamic properties of kerogen: influence of organic type and maturity. Energy Fuel. 29 (1), 91–105. https://doi.org/10.1021/ef502154k.
- Van Duin, A.C.T., Dasgupta, S., Lorant, F., Goddard, W.A., 2001. ReaxFF: a reactive force field for hydrocarbons. J. Phys. Chem. A 105 (41), 9396–9409. https:// doi.org/10.1021/jp004368u.
- Wang, Z., Tang, Y., Wang, Y.L., Zheng, Y., Chen, F., Wu, S., 2020. Kinetics of shale oil generation from kerogen in saline basin and its exploration significance: an example from the Eocene Qianjiang Formation, Jianghan Basin, China. J. Anal. Appl. Pyrol. 150, 104885. https://doi.org/10.1016/j.jaap.2020.104885.
- Wang, J., Liu, Y., Yang, C., Jiang, W., Li, Y., Xiong, Y., 2022. Evolution of mechanical properties of kerogen with thermal maturity. Mar. Petrol. Geol. 145, 105906. https://doi.org/10.1016/j.marpetgeo.2022.105906.
- Xi, K., Li, K., Cao, Y., Lin, M., Niu, X., Zhu, R., 2020. Laminae combination and shale oil enrichment patterns of Chang 73 sub-member organic-rich shales in the Triassic Yanchang Formation, Ordos Basin, NW China. Petrol. Explor. Dev. 47 (6), 1342–1353. https://doi.org/10.1016/S1876-3804(20)60142-8.
- You, Y., Han, X., Wang, X., Jiang, X., 2019. Evolution of gas and shale oil during oil shale kerogen pyrolysis based on structural characteristics. J. Anal. Appl. Pyrol. 138, 203–210. https://doi.org/10.1016/j.jaap.2018.12.025.
- Zhang, C., Jiang, F., Hu, T., Chen, D., Huang, L., Jiang, Z., 2023. Oil occurrence state and quantity in alkaline lacustrine shale using a high-frequency NMR technique.

  Mar. Petrol. Geol. 154, 106302. https://doi.org/10.1016/j.marpetgeo.2023.106302.
- Zhao, X., Zhou, L., Pu, X., Jin, F., Jiang, W., Xiao, D., 2018. Development and exploration practice of the concept of hydrocarbon accumulation in rifted-basin troughs: a case study of Paleogene Kongdian Formation in Cangdong sag, Bohai Bay Basin. Petrol. Explor. Dev. 45 (6), 1166–1176. https://doi.org/10.1016/51876-3804(18)30120-4.
- Zhao, X.Z., Pu, X.G., Zhou, L.H., Jin, F.M., Shi, Z.N., Han, W.Z., Jiang, W.Y., Zhang, W., 2019a. Typical geological characteristics and exploration practices of lacustrine shale oil: a case study of the Kong-2 member strata of the Cangdong Sag in the Bohai Bay Basin. Mar. Petrol. Geol. 113, 103999. https://doi.org/10.1016/j.marpetgeo.2019.08.027.
- Zhao, X., Zhou, L., Pu, X., Han, W., Jin, F., Xiao, D., 2019b. Exploration breakthroughs and geological characteristics of continental shale oil: a case study of the Kongdian Formation in the Cangdong Sag, China. Mar. Petrol. Geol. 102, 544–556. https://doi.org/10.1016/j.marpetgeo.2018.12.020.
- Zhao, X., Zhou, L., Pu, X., Jin, F., Han, W., Shi, Z., 2022. Theories, technologies and practices of lacustrine shale oil exploration and development: a case study of Paleogene Kongdian Formation in Cangdong sag, Bohai Bay Basin, China. Petrol. Phys. Jep. 29, 23, 207–218. https://doi.org/10.1016/518376-3804(22)60059-4.
- Explor. Dev. 49 (3), 707–718. https://doi.org/10.1016/S1876-3804(22)60059-4. Zheng, M., Li, X., Nie, F., Li, G., 2017. Investigation of model scale effects on coal pyrolysis using ReaxFF MD simulation. Mol. Simulat. 43 (13–16), 1081–1088. https://doi.org/10.1080/08927022.2017.1356456.
- Zhou, L., Zhao, X., Chai, G., Jiang, W., Pu, X., Wang, X., 2020. Key exploration & development technologies and engineering practice of continental shale oil: a case study of member 2 of Paleogene Kongdian Formation in Cangdong sag, Bohai Bay Basin, east China. Petrol. Explor. Dev. 47 (5), 1138–1146. https://doi.org/10.1016/S1876-3804(20)60124-0.